

# Dynamical correlations across momentum scales in the Quark–Gluon Plasma

L. Du<sup>1,2</sup> and P. M. Jacobs<sup>1,2</sup>

<sup>1</sup>*Nuclear Science Division, Lawrence Berkeley National Laboratory, Berkeley CA 94270*

<sup>2</sup>*Department of Physics, University of California, Berkeley CA 94270*

(Dated: December 12, 2025)

Experimental probes of the Quark–Gluon Plasma (QGP) generated in heavy–ion collisions span a broad range in momentum scale: low transverse momentum (low  $p_T$ ) measurements probe collective dynamics, while high  $p_T$  measurements probe the response to QGP excitation by jets (jet quenching). However, the dynamical interplay between QGP collective dynamics and jet quenching is currently poorly understood. We present a new framework for exploring dynamical correlations across momentum scales in heavy–ion collisions, based on the  $p_T$ –differential radial-flow observable  $v_0(p_T)$ . Measured  $v_0(p_T)$  phenomenology is traced to the evolution in strength and coherence of distinct underlying fluctuation modes. We then propose new experimental observables to quantify this evolution. The eigenvalue ratio  $\lambda_2/\lambda_1$  of the reference-aligned covariance matrix  $V_0$  is shown to measure the effective fluctuation rank, while the  $p_T$ –dependence of the corresponding eigenvectors maps the evolution from a single coherent soft mode to multi-mode dynamics including coalescence and jet quenching. These observables map the soft–mid–hard correlation structure and provide a unified description of the collective-to-partonic transition in the QGP.

**Introduction.** Strongly-interacting matter at very high temperature and density forms a Quark–Gluon Plasma (QGP), in which quarks and gluons are deconfined [1, 2]. A QGP filled the early universe, and QGP is generated and studied today by the interaction of heavy nuclei at the Relativistic Heavy Ion Collider (RHIC) and the Large Hadron Collider (LHC) [2, 3]. Experimental measurements at these facilities, together with theoretical calculations, show that the dynamical evolution of the QGP exhibits coherent collective flow [4–6], and that the QGP interacts with hard jets and responds to the corresponding excitation (“jet quenching”) [7–9].

These measurements span a broad range in momentum scale. Collective behavior, which is characterized by correlation over a large phase space interval, is probed by particles with “soft” transverse momentum,  $p_T \lesssim 3 \text{ GeV}/c$ . In contrast, jets are generated in high momentum transfer (high  $Q^2$ ) partonic interactions; jet quenching phenomena are typically characterized by particles with “hard”  $p_T \gtrsim 10 \text{ GeV}/c$ , and by measurements of reconstructed jets at high momentum scales. The intermediate  $p_T$  region exhibits phenomena characteristic of a mixture of soft and hard processes, notably quark coalescence [10–14].

Collective flow and jet quenching are usually treated theoretically as distinct phenomena, to simplify their modeling in comparison to data (e.g. [15–21]). Soft anisotropic flow coefficients constrain the bulk geometry and transport properties [22–24], and coalescence studies characterize quark recombination in the intermediate- $p_T$  region [13, 14]. Jet quenching probes the microscopic and coherence structure of the QGP [7–9] and its response to excitation [25–27], and constrain jet transport properties [8, 15, 21].

However, QGP phenomena in these different momentum regimes should be coupled physically; for instance jet quenching is strongly influenced by long–range coherence effects that are the QCD analogue to the Lan-

dau–Pomeranchuk–Migdal effect in QED [9], and the QGP response to jet excitation should have a collective component [28]. An understanding of the dynamical correlation of QGP phenomena at different momentum scales will help elucidate the nature and limits of hydrodynamic collectivity, the mechanisms underlying coalescence, and the constraints on QGP structure and dynamics from jet quenching measurements.

Study of such dynamical correlations requires the measurement of event-by-event fluctuations by an observable that links different momentum scales, quantifying the degree to which the responses at different scales originate from a single collective degree of freedom or from multiple, partially decorrelated dynamical modes. A sensitive and experimentally accessible probe of such correlations is the  $p_T$ –differential radial-flow observable  $v_0(p_T)$  [29, 30],

$$v_0(p_T) = \frac{\langle \delta n(p_T) \delta [p_T]_{\text{ref}} \rangle}{\langle n(p_T) \rangle \sigma_{[p_T]_{\text{ref}}}}, \quad (1)$$

where  $n(p_T)$  is the event-wise normalized particle yield in a narrow bin at momentum  $p_T$ ,  $\delta n(p_T) = n(p_T) - \langle n(p_T) \rangle$ , and  $\langle \dots \rangle$  is the event–ensemble average. The label “ref” indicates a disjoint reference particle sample with event-wise mean transverse momentum  $[p_T]_{\text{ref}}$ , and fluctuations  $\delta [p_T]_{\text{ref}} = [p_T]_{\text{ref}} - \langle [p_T]_{\text{ref}} \rangle$  with variance  $\sigma_{[p_T]_{\text{ref}}}$  relative to the ensemble–averaged distribution. Thus, the numerator measures the covariance between the yield at  $p_T$  and a global momentum scale, while the denominator normalizes this correlation by the average spectrum and the fluctuation amplitude of the reference observable. In experiments, the reference quantities and particle distribution of interest are measured in separated pseudorapidity intervals, to suppress non-flow effects [31, 32].

Anisotropic flow coefficients  $v_n$  are dominated by geometry-driven anisotropies [33, 34], while  $v_0(p_T)$  iso-

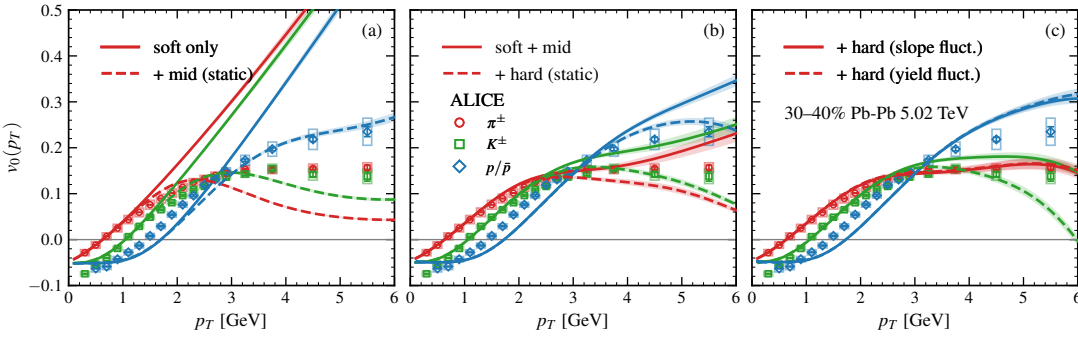


Figure 1. Three-stage construction of  $v_0(p_T)$  for  $\pi^\pm$ ,  $K^\pm$ , and  $p/\bar{p}$  in 30–40% Pb–Pb collisions at  $\sqrt{s_{NN}} = 5.02$  TeV. (a) Soft-only fluctuations (solid) and soft fluctuations with a static mid- $p_T$  component (dashed). (b) Soft+mid fluctuations (solid), augmented by a static hard tail (dashed). (c) Soft+mid+hard fluctuations with slope modulation (solid) or yield modulation (dashed) of the hard component. Shaded bands denote statistical uncertainties from bootstrap resampling. ALICE data from [32].

lates the isotropic component of the event-by-event response and is therefore directly sensitive to radial-flow and spectrum-shape fluctuations. Specifically for this observable, jet quenching corresponds to the suppression of the inclusive particle yield at high  $p_T$  [7–9], and in a hydrodynamic picture mean  $p_T$  is driven by the overall temperature scale of the QGP [4–6]. In this picture,  $v_0(p_T)$  quantifies the event-wise correlation between yield suppression due to quenching and the temperature scale of the medium. Theoretical calculations based on this and other physical pictures can be tested against experimental measurements of  $v_0(p_T)$ .

Recent LHC measurements of  $v_0(p_T)$  reveal a rise–plateau–downturn structure, with species hierarchy and robust low- $p_T$  universality [31, 32]. While these features encode the interplay of soft collectivity, quark recombination, and jet quenching, their dynamical origin remains unclear [35–42].

In this Letter we propose a new framework which directly connects the features of  $v_0(p_T)$  to the number, strength, and coherence of underlying fluctuation modes across soft, intermediate, and hard momentum scales. We demonstrate how the  $v_0(p_T)$  structure observed in LHC measurements arises from a sequence of coherent, partially coherent, and anti-correlated responses, by progressively activating correlated soft, coalescence, and hard components. An eigenmode analysis of the reference-aligned covariance matrix  $V_0(p_{T1}, p_{T2})$  shows that the effective fluctuation rank, quantified for the first time by the eigenvalue ratio  $\lambda_2/\lambda_1$ , provides an “order parameter” for soft–hard decorrelation that counts the effective fluctuation modes.

This framework provides a direct and experimentally accessible means [43, 44] to map the coherence structure linking soft, mid-, and hard momentum sectors across collision systems and beam energies, enabling systematic measurements of soft–mid–hard correlations and the collective–to–partonic transition in heavy-ion collisions.

### Spectrum composition and correlation topology.

We focus in this analysis on the inclusive particle spectrum in the range  $p_T < 15$  GeV/c. The spectrum is modeled as the sum of three overlapping components, each dominant in a different  $p_T$  regime (see Supplemental Material [45]):

$$n(p_T) = n_{\text{soft}}(p_T) + n_{\text{mid}}(p_T) + n_{\text{hard}}(p_T). \quad (2)$$

The soft-sector distribution ( $p_T \lesssim 2$  GeV/c) has a blast-wave form, with parameters corresponding to freeze-out temperature and radial flow [46, 47]. The intermediate  $p_T$  region ( $2 \lesssim p_T \lesssim 5$  GeV/c) is modeled by a recombination-inspired component that remains correlated with the soft background, reflecting their shared hydrodynamic origin. The hard tail ( $p_T \gtrsim 5$  GeV/c) has a power-law form matched continuously to the coalescence region.

Event-by-event fluctuations of the spectrum components are introduced by correlated variation in the soft and mid- $p_T$  parameters, generating partially coherent deformations of their shapes. Hard-sector fluctuations have two quenching-like components: yield modulation that rescales the total yield in the hard region, and slope modulation that varies the power-law index. Together, these fluctuations generate the full soft–mid–hard covariance structure that governs  $v_0(p_T)$  and  $V_0(p_{T1}, p_{T2})$ .

This sequential construction enables a controlled analysis of the contribution of the soft, mid-, and hard-momentum sectors to the particle spectrum  $n(p_T)$  and to  $v_0(p_T)$ , isolating the effects of dilution, soft–mid partial coherence, and soft–hard decorrelation. To make these contributions explicit, the spectrum can be written as  $n(p_T) = n_{\text{soft}}(p_T) + n_{\text{add}}(p_T)$ , where  $n_{\text{add}}$  denotes additional mid- or hard-momentum contributions, with fractional weights  $f_{\text{soft}}(p_T) = \langle n_{\text{soft}}(p_T) \rangle / \langle n(p_T) \rangle$  and  $f_{\text{add}}(p_T) = \langle n_{\text{add}}(p_T) \rangle / \langle n(p_T) \rangle$  that encode the contribution of each sector. The numerator of  $v_0(p_T)$  is the covariance with respect to the reference scale, while the denominator is weighted by the mean yield. For an added component that is uncorrelated with the reference,  $v_0(p_T)$

is reduced by the factor  $f_{\text{soft}}(p_T)$ , corresponding to a dilution of the coherent soft mode. An added component with coherent or anti-coherent fluctuations enhances or suppresses the signal (see Supplemental Material).

Figure 1 shows a buildup of  $v_0(p_T)$  through sequential activation of the soft, mid-, and hard components, separately for pions, kaons, and protons, compared to ALICE data [32]. The event-wise average  $[p_T]_{\text{ref}}$  is calculated using the pion spectrum as a proxy for the charged-hadron distribution. Panel (a) shows only the soft (blast-wave) sector fluctuations (solid); both the monotonic increase in  $v_0(p_T)$  with  $p_T$  and the particle species ordering are consistent with the data for  $p_T \lesssim 1.5 \text{ GeV}/c$  and with hydrodynamic calculations [30, 35–37]. A static mid- $p_T$  component (coalescence-like) increases the denominator of Eq. (1) in the  $2 < p_T < 5 \text{ GeV}/c$  range, thereby flattening  $v_0(p_T)$  (dashed); this is a dilution rather than a genuine dynamical decorrelation.

Figure 1, panel (b), introduces fluctuations in the mid- $p_T$  component, which partially restores the covariance. However, since these fluctuations retain incomplete coherence with the soft background, they generate the plateau over  $2 < p_T < 4 \text{ GeV}/c$  (solid), in contrast to the linear rise produced by a fully coherent soft sector. The observed baryon–meson ordering at mid- $p_T$  follows from recombination, since baryons inherit flow from a larger number of constituent quarks, generating stronger soft–mid correlations. A static hard tail (dashed) suppresses  $v_0(p_T)$ . Because the spectrum  $n(p_T)$  is event-wise normalized, the static hard component acquires a small correlation with the reference through overall multiplicity fluctuations. This effect is purely normalization-induced and likewise does not constitute a genuine soft–hard dynamical coupling.

Finally, Fig. 1, panel (c), introduces event-wise fluctuations in the yield normalization and power-law index (slope) of the hard component. Both effects can arise from jet quenching but generate distinct effects in  $v_0(p_T)$ : slope fluctuations produce a largely uniform flattening, while yield fluctuations produce a marked turnover for kaons. The component ratios (Supplemental Material) show that soft, coalescence, and hard contributions make similar contributions to the kaon spectrum for  $3 < p_T < 5 \text{ GeV}/c$ . In this region the soft–hard anti-correlation due to yield modulation acts in opposition to the positive soft–mid covariance, thereby cancelling the coherent response and suppressing  $v_0(p_T)$  most efficiently for kaons. For pions, the hard tail is dominant only at larger  $p_T$  and the cancellation is weaker. The proton spectrum is largely dominated by the soft component in this range and retains an almost coherent response. The region  $3 < p_T < 5 \text{ GeV}/c$  for kaons thus provides discrimination of the mechanisms underlying hard-sector fluctuations: a strong downturn  $v_0(p_T)$  indicates yield modulation, while a flatter tail corresponds to slope modulation.

Figure 1 maps out the phenomenology of  $v_0(p_T)$  across

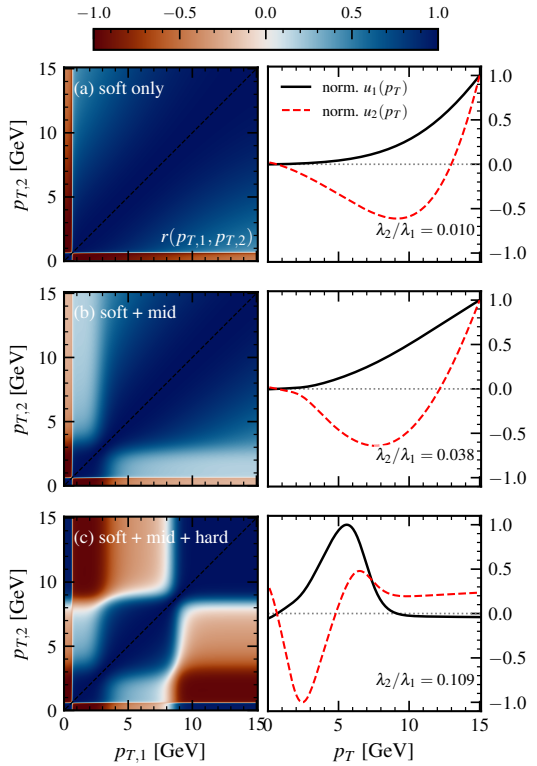


Figure 2. Diagnostics of the reference-aligned covariance matrix  $V_0(p_{T1}, p_{T2})$  for pions. Left panels: two-bin factorization ratio  $r(p_{T1}, p_{T2})$  for (a) soft-only, (b) soft+mid, and (c) soft+mid+hard (slope-modulated) configurations. Right panels: corresponding normalized leading and subleading eigenvectors  $u_1(p_T)$  and  $u_2(p_T)$ , together with the subleading-to-leading eigenvalue ratio  $\lambda_2/\lambda_1$ .

momentum scales, linking the rise–plateau–downturn structure to three distinct correlation regimes. Positive soft–soft covariance underlies the rising low- $p_T$  response; partial soft–mid coherence drives the intermediate plateau; and negative soft–hard covariance, together with dilution from the ensemble-averaged spectrum, drives the high- $p_T$  downturn. This progression provides intuition for how collective, coalescence, and quenching dynamics coexist within an event ensemble, and motivates their quantitative characterization in terms of covariance rank and fluctuation mode structure.

**Fluctuation diagnostics: factorization and rank evolution.** To quantify the strength and mutual correlation of different fluctuation modes as a function of  $p_T$ , we utilize the reference-aligned covariance matrix,

$$V_0(p_{T1}, p_{T2}) = \left\langle [\delta n(p_{T1}) \delta [p_T]_{\text{ref}}] [\delta n(p_{T2}) \delta [p_T]_{\text{ref}}] \right\rangle, \quad (3)$$

where  $\delta [p_T]_{\text{ref}}$  serves as a filter to isolate the spectrum component that co-varies with the reference scale  $[p_T]_{\text{ref}}$ . The diagonal elements satisfy  $V_0(p_T, p_T) \propto v_0(p_T)^2$ , while off-diagonal elements encode the covariance between dif-

ferent  $p_T$  regions, directly probing soft–mid–hard correlations. Full coherence corresponds to factorization, i.e.  $V_0(p_{T1}, p_{T2}) \propto v_0(p_{T1})v_0(p_{T2})$ . Deviations from factorization indicate semi-independent fluctuation modes, analogous to flow-factorization breaking in anisotropic flow PCA analyses [29, 48, 49].

Such effects are quantified using two complementary observables. The factorization ratio,

$$r(p_{T1}, p_{T2}) = \frac{V_0(p_{T1}, p_{T2})}{\sqrt{V_0(p_{T1}, p_{T1})V_0(p_{T2}, p_{T2})}}, \quad (4)$$

maps deviations from a rank-1, fully coherent structure, while the eigenvalue decomposition  $V_0 = \sum_i \lambda_i u_i(p_{T1})u_i(p_{T2})$  identifies the underlying fluctuation components. The leading mode  $u_1(p_T)$  captures the coherent hardening of the spectrum, with additional modes  $u_{2,3,\dots}(p_T)$  becoming significant when new fluctuation sources are active. A genuine new mode produces a distinct  $u_2(p_T)$  together with a rise in the subleading-to-leading eigenvalue ratio  $\lambda_2/\lambda_1$ . The rank structure of  $V_0$  therefore quantifies the emergence and strength of additional dynamical fluctuation modes.

Figure 2 presents these diagnostics for pions. Panel (a), with soft-only fluctuations, exhibits excellent factorization ( $r \simeq 1$ ) and small  $\lambda_2/\lambda_1 \simeq 10^{-2}$ . The leading eigenvector  $u_1(p_T)$  rises monotonically with  $p_T$ , consistent with a single collective hardening mode, with the subleading mode  $u_2(p_T)$  exhibiting only the sign changes required by orthogonality.

Panel (b), including mid- $p_T$  fluctuations, exhibits factorization breaking at  $p_T \gtrsim 3 \text{ GeV}/c$  (left), indicating decorrelation between soft and mid- $p_T$  sectors. Consistently,  $\lambda_2/\lambda_1$  increases fourfold to  $\sim 0.04$ , demonstrating the appearance of a second fluctuation mode. While the overall shape of  $u_2(p_T)$  continues to be dominated by the soft-mode orthogonality pattern, the subleading structure is shifted toward the  $2\text{--}5 \text{ GeV}/c$  region where coalescence fluctuations enter. The form of the dominant mode  $u_1(p_T)$  becomes slightly steeper in  $2 < p_T < 5 \text{ GeV}/c$ , reflecting the redistribution of variance from the soft mode to the semi-independent coalescence-driven mode.

Panel (c), which also includes hard-sector fluctuations, generates a stronger low-to-high- $p_T$  anti-correlation, visible as the red negative band in the factorization map (left), with  $\lambda_2/\lambda_1$  increasing to  $\sim 0.1$ . The subleading eigenvector becomes “tilt-like,” with opposite sign at low and high momentum, indicating a hard-tail fluctuation superimposed on the soft baseline.

Figure 2 reveals a controlled increase in the effective rank of  $V_0$ : a single coherent soft mode, followed by more complex multi-mode dynamics due to mid- and hard-sector variations. The value of  $\lambda_2/\lambda_1$ , which provides a compact metric for the number of active fluctuation modes, encodes this transition. Figure 3 shows  $\lambda_2/\lambda_1$  for  $\pi^\pm$ ,  $K^\pm$ , and  $p/\bar{p}$  for these choices of fluctuation mode.

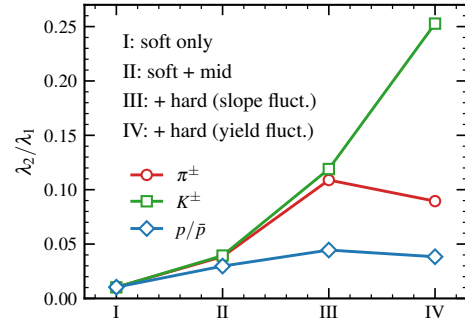


Figure 3. Subleading-to-leading eigenvalue ratio  $\lambda_2/\lambda_1$  for  $\pi^\pm$ ,  $K^\pm$ , and  $p/\bar{p}$  for different sets of fluctuation modes.

For soft-only (case I), all species have  $\lambda_2/\lambda_1 \simeq 0.01$ , reflecting the common single-mode origin. Mid- $p_T$  fluctuations (case II) increase  $\lambda_2/\lambda_1$  for all species and generate a baryon–meson separation, consistent with expectations from coalescence. Hard-sector variations (cases III and IV) increase the ratio more strongly, producing a clear hierarchy  $\lambda_2/\lambda_1(K) > \lambda_2/\lambda_1(\pi) > \lambda_2/\lambda_1(p)$  that reflects the differing degree of soft–mid–hard mixing for each species.

The origin of this kaon enhancement is due to the same factors that shape  $v_0^K(p_T)$  (Fig. 1(c)): the soft, coalescence, and hard contributions to the kaon spectrum are comparable in the region  $3 < p_T < 5 \text{ GeV}/c$ , making  $K^\pm$  especially sensitive to decorrelation of these sectors. The resulting rise in  $\lambda_2/\lambda_1$  reflects this multi-mode structure and demonstrates how the eigenvalue spectrum exposes the physics behind the species-dependent  $v_0(p_T)$  response. The ratio  $\lambda_2/\lambda_1$  is therefore a structural counterpart to  $v_0(p_T)$ , providing an experimentally accessible indicator of how multiple fluctuation modes contribute across  $p_T$ .

**Experimental considerations.** The quantities  $V_0(p_{T1}, p_{T2})$ ,  $r(p_{T1}, p_{T2})$ , and  $\lambda_2/\lambda_1$ , are experimentally measurable, using techniques similar to those used for measuring high-order flow harmonics [48–52]. However, their measurement with good statistical precision is limited in range at high  $p_T$ , due to the sharply falling inclusive particle production spectrum [53–55]. Current measurements of charged-particle  $v_0(p_T)$  for Pb–Pb collisions at  $\sqrt{s_{\text{NN}}} = 5.02 \text{ TeV}$  [31, 32] and Au–Au collisions at  $\sqrt{s_{\text{NN}}} = 200 \text{ GeV}$  [56] extend to  $p_T \sim 10 \text{ GeV}/c$  with good precision, well into the region where hard modes are expected to dominate, enabling the analysis program outlined here.

This momentum reach covers the region of primary interest for species-resolved measurements,  $2 < p_T < 5 \text{ GeV}/c$  region, where our framework predicts the largest mode-dependent differences, most notably for kaons. This approach may also be applicable to RHIC Beam Energy Scan data [57–60], where the relative strength of soft, coalescence, and Cronin scattering [61] contributions is expected to evolve rapidly with  $\sqrt{s_{\text{NN}}}$ .

**Summary.** We have presented a new framework to measure the interplay of the mechanisms underlying particle production in collider measurements of the QGP: collective flow, partonic coalescence, and jet quenching. The framework is based on the radial flow fluctuation observable  $v_0(p_T)$ , which correlates event-by-event fluctuations at various momentum scales with those of a reference quantity that characterizes the event structure as a whole. The observable  $v_0(p_T)$  provides a momentum-differential probe of event-by-event fluctuations, characterizing the contribution of different underlying mechanisms as a function of scale.

This framework is explored using a simplified model of heavy-ion collisions that incorporates fluctuations in soft hydrodynamic emission, quark recombination, and quenched hard fragments. The model reproduces the rise–plateau–downturn structure and species hierarchy of  $v_0(p_T)$  observed in LHC data, showing how coherent soft response, partially coherent coalescence, and decorrelated or anti-correlated hard modes combine across momentum scales.

Analysis of the factorization ratio  $r(p_{T1}, p_{T2})$  and the eigenvalue spectrum of the reference-aligned covariance matrix  $V_0$  demonstrates that the transition from soft coherence to multi-mode dynamics is signalled by the growth of the subleading-to-leading eigenvalue ratio  $\lambda_2/\lambda_1$ . This ratio serves as an experimentally accessible order parameter, counting the number of active fluctuation modes and providing a quantitative metric of the underlying soft-hard correlation topology. This mode-based picture also clarifies characteristic patterns of  $v_0(p_T)$  measurements across systems, centralities, and energies. In particular, the observed low- $p_T$  universality of  $v_0(p_T)$ , both in shape and in  $p_T/\langle p_T \rangle$  scaling, follows directly from the dominance of a single soft fluctuation mode [62].

These results establish  $v_0(p_T)$  as a sensitive and experimentally accessible probe of the interplay of collective modes of excitation, partonic coalescence, and jet quenching in the QGP, a long-standing goal in the field. Measurement of the proposed observables will quantify the correlation topology linking collective and partonic physics in the QGP.

**Acknowledgements.** This work was supported by the US Department of Energy, Office of Science, Office of Nuclear Physics under grant number DE-AC02-05CH11231.

- 
- [1] E. Shuryak, *Rev. Mod. Phys.* **89**, 035001 (2017), [arXiv:1412.8393 \[hep-ph\]](#).
- [2] W. Busza, K. Rajagopal, and W. van der Schee, *Ann. Rev. Nucl. Part. Sci.* **68**, 339 (2018), [arXiv:1802.04801 \[hep-ph\]](#).

- [3] J. W. Harris and B. Müller, *Eur. Phys. J. C* **84**, 247 (2024), [arXiv:2308.05743 \[hep-ph\]](#).
- [4] U. Heinz and R. Snellings, *Ann. Rev. Nucl. Part. Sci.* **63**, 123 (2013), [arXiv:1301.2826 \[nucl-th\]](#).
- [5] C. Gale, S. Jeon, and B. Schenke, *Int. J. Mod. Phys. A* **28**, 1340011 (2013), [arXiv:1301.5893 \[nucl-th\]](#).
- [6] P. Huovinen and P. V. Ruuskanen, *Ann. Rev. Nucl. Part. Sci.* **56**, 163 (2006), [arXiv:nucl-th/0605008](#).
- [7] L. Cunqueiro and A. M. Sickles, *Prog. Part. Nucl. Phys.* **124**, 103940 (2022), [arXiv:2110.14490 \[nucl-ex\]](#).
- [8] L. Apolinário, Y.-J. Lee, and M. Winn, *Prog. Part. Nucl. Phys.* **127**, 103990 (2022), [arXiv:2203.16352 \[hep-ph\]](#).
- [9] X.-N. Wang and U. A. Wiedemann (2025) [arXiv:2508.18794 \[hep-ph\]](#).
- [10] R. J. Fries, B. Muller, C. Nonaka, and S. A. Bass, *Phys. Rev. Lett.* **90**, 202303 (2003), [arXiv:nucl-th/0301087](#).
- [11] V. Greco, C. M. Ko, and P. Levai, *Phys. Rev. Lett.* **90**, 202302 (2003), [arXiv:nucl-th/0301093](#).
- [12] D. Molnar and S. A. Voloshin, *Phys. Rev. Lett.* **91**, 092301 (2003), [arXiv:nucl-th/0302014](#).
- [13] R. J. Fries, V. Greco, and P. Sorensen, *Ann. Rev. Nucl. Part. Sci.* **58**, 177 (2008), [arXiv:0807.4939 \[nucl-th\]](#).
- [14] F. Becattini and R. Fries, *Landolt-Bornstein* **23**, 208 (2010), [arXiv:0907.1031 \[nucl-th\]](#).
- [15] K. M. Burke *et al.* (JET), *Phys. Rev. C* **90**, 014909 (2014), [arXiv:1312.5003 \[nucl-th\]](#).
- [16] D. Everett *et al.* (JETSCAPE), *Phys. Rev. Lett.* **126**, 242301 (2021), [arXiv:2010.03928 \[hep-ph\]](#).
- [17] D. Everett *et al.* (JETSCAPE), *Phys. Rev. C* **103**, 054904 (2021), [arXiv:2011.01430 \[hep-ph\]](#).
- [18] G. Nijs, W. van der Schee, U. Gürsoy, and R. Snellings, *Phys. Rev. C* **103**, 054909 (2021), [arXiv:2010.15134 \[nucl-th\]](#).
- [19] G. Nijs, W. van der Schee, U. Gürsoy, and R. Snellings, *Phys. Rev. Lett.* **126**, 202301 (2021), [arXiv:2010.15130 \[nucl-th\]](#).
- [20] J. Casalderrey-Solana, Z. Hulcher, G. Milhano, D. Pablos, and K. Rajagopal, *Phys. Rev. C* **99**, 051901 (2019), [arXiv:1808.07386 \[hep-ph\]](#).
- [21] R. Ehlers *et al.* (JETSCAPE), *Phys. Rev. C* **111**, 054913 (2025), [arXiv:2408.08247 \[hep-ph\]](#).
- [22] P. Romatschke and U. Romatschke, *Phys. Rev. Lett.* **99**, 172301 (2007), [arXiv:0706.1522 \[nucl-th\]](#).
- [23] U. W. Heinz, *Landolt-Bornstein* **23**, 240 (2010), [arXiv:0901.4355 \[nucl-th\]](#).
- [24] H. Song, S. A. Bass, U. Heinz, T. Hirano, and C. Shen, *Phys. Rev. Lett.* **106**, 192301 (2011), [Erratum: *Phys. Rev. Lett.* 109, 139904 (2012)], [arXiv:1011.2783 \[nucl-th\]](#).
- [25] S. Chatrchyan *et al.* (CMS), *Phys. Rev. C* **84**, 024906 (2011), [arXiv:1102.1957 \[nucl-ex\]](#).
- [26] S. Acharya *et al.* (ALICE), *Phys. Rev. Lett.* **133**, 022301 (2024), [arXiv:2308.16131 \[nucl-ex\]](#).
- [27] B. E. Aboona *et al.* (STAR), (2025), [arXiv:2505.05789 \[nucl-ex\]](#).
- [28] S. Cao and G.-Y. Qin, *Ann. Rev. Nucl. Part. Sci.* **73**, 205 (2023), [arXiv:2211.16821 \[nucl-th\]](#).
- [29] F. G. Gardim, F. Grassi, P. Ishida, M. Luzum, and J.-Y. Ollitrault, *Phys. Rev. C* **100**, 054905 (2019), [arXiv:1906.03045 \[nucl-th\]](#).
- [30] B. Schenke, C. Shen, and D. Teaney, *Phys. Rev. C* **102**, 034905 (2020), [arXiv:2004.00690 \[nucl-th\]](#).
- [31] G. Aad *et al.* (ATLAS), (2025), [arXiv:2503.24125 \[nucl-ex\]](#).

- [32] S. Acharya *et al.* (ALICE), (2025), arXiv:2504.04796 [nucl-ex].
- [33] S. A. Voloshin, A. M. Poskanzer, and R. Snellings, *Landolt-Bornstein* **23**, 293 (2010), arXiv:0809.2949 [nucl-ex].
- [34] U. Heinz, Z. Qiu, and C. Shen, *Phys. Rev. C* **87**, 034913 (2013), arXiv:1302.3535 [nucl-th].
- [35] T. Parida, R. Samanta, and J.-Y. Ollitrault, *Phys. Lett. B* **857**, 138985 (2024), arXiv:2407.17313 [nucl-th].
- [36] S. A. Jahan, H. Roch, and C. Shen, (2025), arXiv:2507.11394 [nucl-th].
- [37] L. Du, (2025), arXiv:2508.07184 [hep-ph].
- [38] J. Jia, (2025), arXiv:2507.14399 [nucl-th].
- [39] S. Bhattacharya, A. Dimri, and J. Jia, (2025), arXiv:2504.20008 [nucl-th].
- [40] S. Saha, R. Singh, and B. Mohanty, *Phys. Rev. C* **112**, 024902 (2025), arXiv:2505.19697 [nucl-ex].
- [41] M. L. Sambataro, S. Plumari, S. K. Das, and V. Greco, (2025), arXiv:2510.19448 [hep-ph].
- [42] J. Wan, C.-Z. Wang, Y.-G. Ma, and Q.-Y. Shou, (2025), arXiv:2509.24889 [nucl-th].
- [43] J. Jia and S. Mohapatra, *Phys. Rev. C* **88**, 014907 (2013), arXiv:1304.1471 [nucl-ex].
- [44] G. Aad *et al.* (ATLAS), *Eur. Phys. J. C* **74**, 3157 (2014), arXiv:1408.4342 [hep-ex].
- [45] See Supplemental Material at [URL will be inserted by publisher] for a brief description of more technical details of this study.
- [46] E. Schnedermann, J. Sollfrank, and U. W. Heinz, *Phys. Rev. C* **48**, 2462 (1993), arXiv:nucl-th/9307020.
- [47] S. Acharya *et al.* (ALICE), *Phys. Rev. C* **101**, 044907 (2020), arXiv:1910.07678 [nucl-ex].
- [48] R. S. Bhalerao, J.-Y. Ollitrault, S. Pal, and D. Teaney, *Phys. Rev. Lett.* **114**, 152301 (2015), arXiv:1410.7739 [nucl-th].
- [49] A. Mazeliauskas and D. Teaney, *Phys. Rev. C* **93**, 024913 (2016), arXiv:1509.07492 [nucl-th].
- [50] K. Aamodt *et al.* (ALICE), *Phys. Lett. B* **708**, 249 (2012), arXiv:1109.2501 [nucl-ex].
- [51] S. Chatrchyan *et al.* (CMS), *JHEP* **07**, 076 (2011), arXiv:1105.2438 [nucl-ex].
- [52] B. Abelev *et al.* (ALICE), *Phys. Lett. B* **719**, 29 (2013), arXiv:1212.2001 [nucl-ex].
- [53] J. Adams *et al.* (STAR), *Phys. Rev. Lett.* **91**, 172302 (2003), arXiv:nucl-ex/0305015.
- [54] V. Khachatryan *et al.* (CMS), *JHEP* **04**, 039 (2017), arXiv:1611.01664 [nucl-ex].
- [55] S. Acharya *et al.* (ALICE), *JHEP* **11**, 013 (2018), arXiv:1802.09145 [nucl-ex].
- [56] A. Tamis, “STAR Overview IS25,” <https://indico.cern.ch/event/1479384/contributions/6562161/>.
- [57] B. I. Abelev *et al.* (STAR), *Phys. Rev. C* **79**, 034909 (2009), arXiv:0808.2041 [nucl-ex].
- [58] L. Adamczyk *et al.* (STAR), *Phys. Rev. C* **96**, 044904 (2017), arXiv:1701.07065 [nucl-ex].
- [59] A. Bzdak, S. Esumi, V. Koch, J. Liao, M. Stephanov, and N. Xu, *Phys. Rept.* **853**, 1 (2020), arXiv:1906.00936 [nucl-th].
- [60] L. Du, A. Sorensen, and M. Stephanov, *Int. J. Mod. Phys. E* **33**, 2430008 (2024), arXiv:2402.10183 [nucl-th].
- [61] D. Antreasyan, J. W. Cronin, H. J. Frisch, M. J. Shochet, L. Kluberg, P. A. Piroue, and R. L. Sumner, *Phys. Rev. D* **19**, 764 (1979).
- [62] A fuller discussion of these universality features and their connection to the soft-mode structure will be presented in a forthcoming extended study.

## SUPPLEMENTAL MATERIAL

### Decoding $v_0(p_T)$ : composition, correlations, and fluctuation rank

The analytic structure of  $v_0(p_T)$  may be understood through three connected layers: (a) the weighted composition of the spectrum, (b) its mapping to underlying inter-sector correlations, and (c) the fluctuation rank of the associated covariance matrix. These relations hold independent of model details and provide the theoretical basis for the interpretation of the results in the main text.

*Weighted composition.* Because  $v_0(p_T)$  depends on both the covariance (numerator) and the mean yield (denominator), a flattening of  $v_0(p_T)$  does not necessarily indicate a loss of soft correlations—it may simply reflect dilution from an additional, weakly correlated yield component. Consider a two-component spectrum with a fluctuating soft contribution  $n_s(p_T)$  and a static or weakly correlated component  $n_x(p_T)$ , such that  $n(p_T) = n_s(p_T) + n_x(p_T)$ . The measured fluctuation becomes

$$v_0(p_T) = \sum_{k=s,x} f_k(p_T) v_0^{(k)}(p_T), \quad (1)$$

where

$$f_k(p_T) = \frac{\langle n_k(p_T) \rangle}{\langle n_s(p_T) + n_x(p_T) \rangle}, \quad (2)$$

a weighted sum of the intrinsic sector responses  $v_0^{(k)}(p_T)$ . If the added source is uncorrelated with the reference ( $v_0^{(x)} \simeq 0$ ),

$$v_0(p_T) \simeq f_s(p_T) v_0^{(s)}(p_T), \quad (3)$$

corresponding to pure dilution of the coherent soft mode. Partially correlated or anti-correlated components modify the numerator as well, producing precisely the rise–plateau–downturn structure observed in experiment. This compact formulation directly links the observed  $v_0(p_T)$  to the underlying spectral composition.

*Covariance matrix and fluctuation rank.* The covariance matrix of normalized yield fluctuations,

$$V_0(p_{T1}, p_{T2}) = \frac{\langle \delta n(p_{T1}) \delta n(p_{T2}) \rangle}{\langle n(p_{T1}) \rangle \langle n(p_{T2}) \rangle}, \quad (4)$$

reveals the number of independent fluctuation drivers through its eigen-decomposition

$$V_0(p_{T1}, p_{T2}) = \sum_i \lambda_i u_i(p_{T1}) u_i(p_{T2}), \quad (5)$$

which defines orthogonal modes  $u_i(p_T)$  with strengths  $\lambda_i$ . A nearly factorized (rank-1) matrix corresponds to a single coherent soft mode, while partially decorrelated

mid- or hard-sector variations generate subleading eigenvalues  $\lambda_{2,3,\dots}$ . The ratio  $R_{\text{rank}} \equiv \lambda_2/\lambda_1$  therefore provides a compact and quantitative diagnostic of fluctuation dimensionality.

Physically,  $u_1(p_T)$  represents the global hardening deformation driven by collective flow; a subleading  $u_2(p_T)$  localized near 2–5 GeV reflects coalescence-type fluctuations, whereas a low–high  $p_T$  sign change signals soft–hard anti-correlation.

In the main analysis we employ the *reference-aligned* covariance, constructed from the projected fluctuations  $\delta n(p_T) \delta[p_T]_{\text{ref}}$  so that it isolates the part of the spectrum that fluctuates coherently with the soft reference in  $v_0(p_T)$ . This aligned covariance enhances coherent contributions but retains the same eigenvector structure and rank ordering as the normalized covariance. The factorization ratio

$$r(p_{T1}, p_{T2}) = \frac{V_0(p_{T1}, p_{T2})}{\sqrt{V_0(p_{T1}, p_{T1}) V_0(p_{T2}, p_{T2})}}, \quad (6)$$

provides a complementary measure of local correlations:  $r \simeq 1$  indicates a single coherent (rank-1) mode,  $0 < r < 1$  signals partial decorrelation, and  $r < 0$  indicates anti-correlation between momentum regions. A combined analysis of  $r(p_{T1}, p_{T2})$  and  $R_{\text{rank}}$  thus pinpoints where factorization breaks and how many fluctuation modes contribute.

### Spectral framework and fluctuations

To model these mechanisms quantitatively, the transverse-momentum distribution ( $p_T < 15$  GeV) is represented as a superposition of three physically motivated sectors—a soft blast-wave baseline, an intermediate coalescence bridge, and a hard fragmentation tail—each corresponding to a distinct microscopic regime. The inclusive spectrum

$$\frac{dN}{p_T dp_T} = [N_{\text{soft}} S(p_T) + N_{\text{mid}} C(p_T) + N_{\text{hard}} H(p_T)], \quad (7)$$

uses normalized component shapes  $S$ ,  $C$ , and  $H$  with smooth transitions around  $p_T \simeq 2$  and 5 GeV. The soft component follows an isotropic blast-wave form with kinetic temperature  $T_{\text{kin}}$ , surface velocity  $\beta_s$ , and profile exponent  $n$ ,

$$S(p_T) \propto \int_0^1 ds s m_T I_0\left(\frac{p_T \sinh \rho_T}{T_{\text{kin}}}\right) K_1\left(\frac{m_T \cosh \rho_T}{T_{\text{kin}}}\right),$$

where  $\rho_T = \tanh^{-1}(\beta_s s^n)$  and  $m_T = \sqrt{p_T^2 + m^2}$ . The coalescence component employs an effective quark kernel  $f_q(p_T) \propto p_T^{a_q} \exp[-p_T/T_q^{\text{eff}}]$  with  $T_q^{\text{eff}} = T_q(\beta_{\text{eff}}/\beta_{\text{ref}})^\eta$ , leading to

$$C_h(p_T) \propto [f_q(p_T/n_q; a_q, T_q, \eta, \beta_{\text{ref}})]^{n_q} \left(1 + \frac{p_T}{p_s}\right)^{-\delta},$$

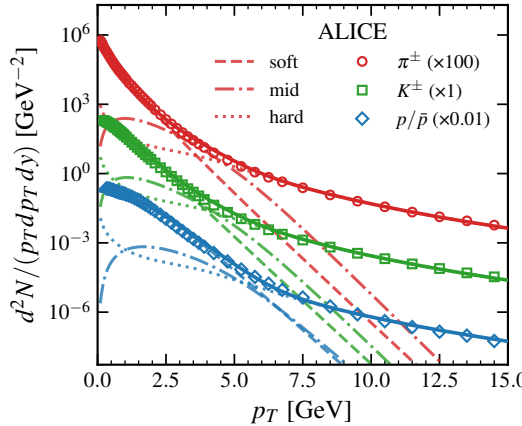


Figure 1. Inclusive transverse-momentum spectra of  $\pi^\pm$ ,  $K^\pm$ , and  $p/\bar{p}$  in 30–40% Pb–Pb collisions at  $\sqrt{s_{NN}} = 5.02$  TeV compared with the three-component model. Solid curves show the total spectra, while others indicate the soft, mid- $p_T$  (coalescence-like), and hard (fragmentation-like) components.

while the high- $p_T$  tail is described by a quenched power law

$$H(p_T) \propto p_T^{-1} (1 + p_T/p_0)^{-n_0}.$$

Event-by-event fluctuations are introduced by correlated variations of  $(\beta_s, \beta_{\text{mid}}, T_{\text{kin}}, T_q)$  drawn from a four-dimensional multivariate normal distribution with covariances  $\rho_{\beta T}^{(\text{soft})} = \text{Corr}(\beta_s, T_{\text{kin}})$ ,  $\rho_{\beta T}^{(\text{mid})} = \text{Corr}(\beta_{\text{mid}}, T_q)$ , and  $\rho_{\text{sm}} = \text{Corr}(\beta_s, \beta_{\text{mid}})$ . Each draw defines one event, evaluated consistently for all sectors, and two slightly decorrelated subevents are generated to mimic the experimental  $\eta$ -subevent method and suppress self-correlations. The two subevents share the same underlying event parameters but include independent statistical noise, ensuring that the reference quantity used in  $v_0(p_T)$  is decorrelated from the particle of interest.

Quenching-like fluctuations are introduced through two deterministic schemes that couple the hard yield to the soft background. In the amplitude modulation mode, the hard component scales as  $H'(p_T) = A H(p_T)$  with  $A = 1 + \sigma_A (w_\beta \Delta \beta / \beta_0 + w_T \Delta T / T_0)$ , representing global yield suppression or enhancement correlated with the soft flow. In the slope modulation mode, the power-law index fluctuates as  $n_{\text{eff}} = n_0 [1 + \sigma_n (w_\beta \Delta \beta / \beta_0 + w_T \Delta T / T_0)]$ , yielding  $H'(p_T) \propto (1 + p_T/p_0)^{-n_{\text{eff}}}$  after normalization. Both prescriptions provide controlled soft–hard linkages: amplitude modulation generates an anti-correlated

change in the hard yield relative to the soft flow, while slope modulation produces a partially correlated tilt of the hard tail without altering its normalization. The default analysis adopts the slope–modulation configuration, where the hard index responds primarily to the soft velocity ( $w_\beta = 2.0$ ,  $w_T = 0$ ) with a fractional width  $\sigma_n = 0.1$ . Together, these prescriptions enable tunable soft–hard correlations and quantify how coherent, partially correlated,

Table I. Representative baseline and fluctuation parameters of the three-component model.

Component	Parameter	Symbol	Value
Soft	Kinetic temperature [GeV]	$T_{\text{kin}}$	0.094
	Surface velocity	$\beta_s$	0.897
	Profile exponent	$n$	0.739
	Dispersion of $\beta_s$	$\sigma_{\beta_s}$	0.012
	Dispersion of $T_{\text{kin}}$ [GeV]	$\sigma_{T_{\text{kin}}}$	0.002
	Intra-sector corr.	$\rho_{\beta T}^{(\text{soft})}$	-0.5
Mid	Quark slope [GeV]	$T_q$	0.36
	Flow exponent	$\eta$	1.8
	Reference velocity	$\beta_{\text{ref}}$	0.65
	Tail scale [GeV]	$p_s$	4.7
	Tail exponent	$\delta$	1.2
	Dispersion of $\beta_{\text{mid}}$	$\sigma_{\beta_{\text{mid}}}$	0.04
Hard	Dispersion of $T_q$ [GeV]	$\sigma_{T_q}$	0.03
	Intra-sector corr.	$\rho_{\beta T}^{(\text{mid})}$	-0.55
	Inter-sector corr.	$\rho_{\text{sm}}$	0.5
	Scale [GeV]	$p_0$	2.0
	Power index	$n_0$	5.8
	Slope fluctuation width	$\sigma_n$	0.1
	Velocity coupling weight	$w_\beta$	2.0
	Temperature coupling weight	$w_T$	0.0

and anti-correlated modes shape  $v_0(p_T)$  and  $V_0(p_{T1}, p_{T2})$ .

Event-by-event variations of the soft and mid- $p_T$  parameters are drawn from a correlated Gaussian ensemble characterized by  $\sigma_{\beta_s} = 0.012$ ,  $\sigma_{T_{\text{kin}}} = 0.002$ , and  $\rho_{\beta T}^{(\text{soft})} = -0.5$  for the soft sector, and  $\sigma_{\beta_{\text{mid}}} = 0.04$ ,  $\sigma_{T_q} = 0.03$ , and  $\rho_{\beta T}^{(\text{mid})} = -0.55$  for the coalescence sector. The inter-sector correlation between soft and mid flow velocities is set to  $\rho_{\text{sm}} = 0.5$ .

Table I lists representative baseline parameters for all three sectors and their corresponding fluctuation widths and correlations. Values are chosen to reproduce generic LHC Pb–Pb spectra and  $v_0(p_T)$ . The resulting decomposition of the spectra is shown in Fig. 1, which captures the measured slopes and illustrates the successive dominance of soft, mid, and hard contributions that underlie the fluctuation analysis in the main text.